JACS
JOURNAL OF THE AMERICAN CHEMICAL SOCIETY
Article
pubs.acs.org/JACS

"Roller-Wheel"-Type Pt-Containing Small Molecules and the Impact of "Rollers" on Material Crystallinity, Electronic Properties, and Solar Cell Performance

Wenhan He,[#] Maksim Y. Livshits,[#] Diane A. Dickie,[#,†] Zhen Zhang,[#] Luis E. Mejiaortega,[#] Jeffrey J. Rack,[*,#] Qin Wu,[*,Δ] and Yang Qin[*,#]

[#]Department of Chemistry & Chemical Biology, University of New Mexico, Albuquerque, New Mexico 87131, United States
[Δ]Center for Functional Nanomaterials, Brookhaven National Laboratory, Upton, New York 11973, United States

Supporting Information

ABSTRACT: We report the synthesis, characterization, and detailed comparison of a series of novel Pt-bisacetylide containing conjugated small molecules possessing an unconventional "roller-wheel" shaped structure that is distinctly different from the "dumbbell" designs in traditional Pt-bisacetylide containing conjugated polymers and small molecules. The relationships between the chemical nature and length of the "rollers" and the electronic and physical properties of the materials are carefully studied by steady-state spectroscopy, cyclic voltammetry, differential scanning calorimetry, single-crystal X-ray diffraction, transient absorption spectroscopy, theoretical calculation, and device application. It was revealed that if the roller are long enough, these molecules can "slip-stack" in the solid state, leading to high crystallinity and charge mobility. Organic solar cells were fabricated and showed power conversion efficiencies up to 5.9%, out-performing all existing Pt-containing materials. The device performance was also found to be sensitive to optimization conditions and blend morphologies, which are a result of the intricate interplay among materials crystallinity, phase separation, and the relative positions of the lowest singlet and triplet excited states.

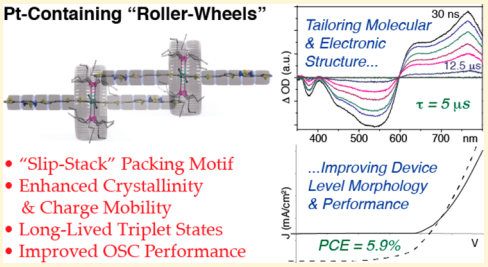

1. INTRODUCTION

Since the discovery of metallic conductivity in doped polyacetylenes, conjugated polymers (CPs) and small molecules (SMs) have evolved into a major research field, and basic understandings in materials synthesis and physical and electronic properties, as well as applications in electronic devices, have advanced rapidly in recent years.[1] Great attention has been focused on synthetic methodology development and understanding of structure−property relationship of conjugated materials by systematically designing and varying the materials' chemical structures. Most such efforts involve organic building blocks and transformations, for example, the construction of low bandgap CPs and SMs by combinations of different electron-rich and electron-poor organic moieties, resulting in the so-called push−pull systems.[2] Although relatively less studied, conjugated materials containing transition metals (TMs) as part of the conjugation system are especially intriguing because of the potential to combine the attractive properties from both organic materials and metals in a constructive manner, as well as to generate emerging new phenomena not observed individually.[3] Among the many examples of TM-containing CPs and SMs, those containing Pt-bisacetylide complexes have been extensively studied for applications in organic solar cells (OSCs) that have been considered low-cost and portable alternative energy sources.[4] The square planar geometry of Pt-bisacetylide complexes offers a facile platform for constructing linear CPs and small molecules, and the large spin−orbit coupling constant of heavy Pt atoms induces efficient intersystem crossing (ISC) and generation of long-lived triplet excitons that have been considered beneficial for OSC operation.[5] Besides a handful of low bandgap Pt-containing CPs that displayed respectable power conversion efficiencies (PCEs) up to ca. 4% in OSC devices,[6] most other examples are relatively inefficient materials with OSC PCEs limited to ca. 1−2%.[7]

A close look at the structures of most existing Pt-bisacetylide containing CPs and SMs reveals that they all possess dumbbell-shaped geometries as schematically shown in Scheme 1A, which feature linear multiaromatic chromophores, typically of push−pull structures, sandwiched between two bulky Pt-bisacetylide complexes. Because of steric constraints, these "dumbbell" structures are not capable of efficient $\pi-\pi$ stacking between adjacent organic chromophores and, as a result, the existing examples of Pt-bisacetylide containing CPs are exclusively amorphous in nature. Such lack of crystallinity leads to weak intermolecular electronic communication and low charge mobility, both of which are detrimental to device performance.

We have recently proposed an alternative "roller-wheel" design (Scheme 1B) by attaching the Pt-bisacetylide moieties

Received: June 8, 2017
Published: July 21, 2017

DOI: 10.1021/jacs.7b05801
J. Am. Chem. Soc. 2017, 139, 14109−14119

Scheme 1. Project Overview

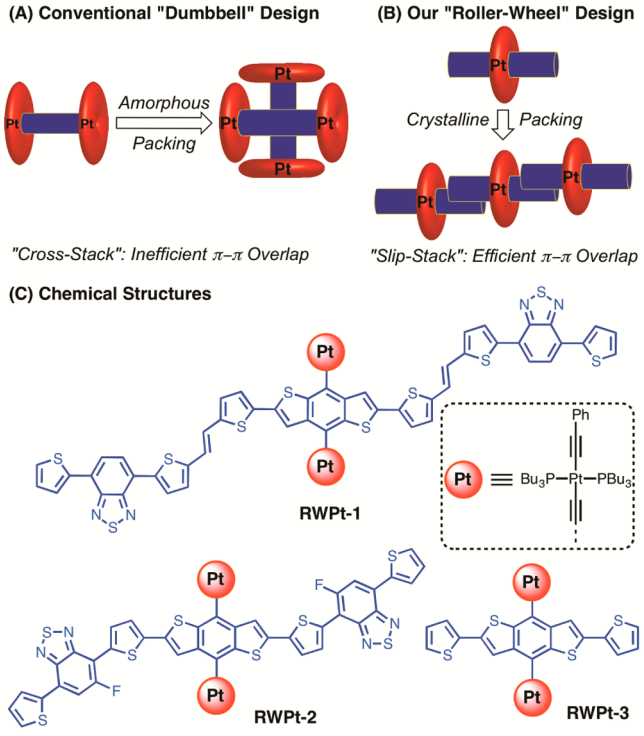

to the short axis of a linear organic chromophore. Such structural motif can allow partial overlap among adjacent chromophores through a "slip-stack" fashion, potentially enhancing material crystallinity and charge mobility. Accordingly, we have synthesized roller-wheel SMs **RWPt-2** and **RWPt-3**, as shown in Scheme 1C.[8] Single crystals of **RWPt-3** were obtained but showed no $\pi-\pi$ interactions between organic chromophores, which resulted in poor OSC performance. On the other hand, **RWPt-2** displayed much reduced bandgap and enhanced intermolecular interactions when compared with **RWPt-3**, although no single crystals could be obtained to definitively prove the slip-stack geometry. OSC devices employing **RWPt-2** generated PCEs of ~5–6%, outperforming all existing Pt-containing CPs and SMs. We rationalize that the differences in physical and electronic properties of **RWPt-2** and **RWPt-3** originate from the different lengths of "rollers", i.e., the linear organic chromophores. Thus, fine-tuning the lengths and structures of the roller offers a facile platform for better understanding of the structure–property relationship of this new class of roller-wheel Pt-containing materials. In this paper, we describe the synthesis, characterization, and OSC application of **RWPt-1** (Scheme 1C) having a more extended roller length. Single crystals of **RWPt-1** unambiguously confirm the slip-stack geometries in the solid state. Detailed comparisons among the physical and electronic properties of **RWPt-1**, **RWPt-2**, and **RWPt-3** are carried out, which reveal useful insights on the determining effects of roller characteristics over materials crystallinity, bandgap, excited-state dynamics, and device performance.

2. EXPERIMENTAL SECTION

Materials and General Methods. All reagents and solvents were used as received from Sigma-Aldrich or VWR unless otherwise noted. Anhydrous THF was distilled over Na/benzophenone prior to use. Anhydrous chloroform and triethylamine (TEA) were obtained by distillation over CaH_2 and degassed through several freeze–pump–thaw cycles. Phenyl-C_{61}-butyric acid methyl ester ($PC_{61}BM$) and phenyl-C_{71}-butyric acid methyl ester ($PC_{71}BM$) were purchased from American Dye Source. *N*,*N*-Diethyl-3-thiophenecarboxamide (**1**),[9] benzo[1,2-*b*:4,5-*b*′]dithiophene-4,8-dione (**2**),[10] benzo[1,2-*b*:4,5-*b*′]-dithiophene-4,8-bis[2-[triisopropylsilyl]ethynyl] (**3**),[11] 2,6-dibromo-4,8-bis[2-[triisopropylsilyl]ethynyl] (**4**),[12] *trans*-chloro-(phenylethynyl)bis(tributylphosphine)platinum (**7**),[13] 4,7-di-2-thienyl-2,1,3-benzothiadiazole (**9**),[14] 5-[7-(2-thienyl)-2,1,3-benzothiadiazol-4-yl]-2-thiophenecarboxaldehyde (**10**),[15] and 5-[7-(2-thienyl)-2,1,3-benzothiadiazol-4-yl]-2-thiophenemethanol (**11**)[16] were synthesized according to literature procedures. The 300.13 MHz ^{1}H, 75.48 MHz ^{13}C, 121.5 MHz ^{31}P spectra were recorded on a Bruker Avance III Solution 300 spectrometer. All solution ^{1}H spectra were referenced internally to tetramethylsilane, and ^{13}C spectra were referenced internally to chloroform. ^{31}P was referenced externally by using standard H_3PO_4 (δ = 0 ppm). Ultraviolet visible (UV–vis) absorption spectra were recorded on a Shimadzu UV-2401 PC spectrometer over a wavelength range of 300–900 nm. Fluorescence emission spectra were obtained using a Varian Cary Eclipse fluorimeter. Differential scanning calorimetry (DSC) measurements were performed on a Mettler Toledo DSC STARe system with ca. 8–10 mg sample and at a scan rate of 10 °C/min. The results reported are from the second heating cycle. Cyclic voltammetry (CV) was performed at 25 °C on a CH Instrument CHI604xD electrochemical analyzer using a glassy carbon working electrode, a platinum wire counter electrode, and a Ag/AgCl reference electrode, calibrated using a ferrocene redox couple (4.8 eV below vacuum). Single-crystal X-ray diffraction (XRD) data were collected on a Bruker Kappa APEXII CCD system equipped with a graphite monochromator and a Mo Kα fine-focus tube (λ = 0.71073 Å). The frames were integrated with the Bruker SAINT software package using a narrow-frame algorithm. Data were corrected for absorption effects using the multi-scan method (SADABS). The structure was solved and refined using the Bruker SHELXTL software package. Non-hydrogen atoms were refined anisotropically, except for the chlorobenzene solvent which was refined isotropically without hydrogen atoms. Several butyl groups were found to be disordered over two positions. The occupancy of the disorder was freely refined with constraints on the C–C bond lengths and thermal parameters of the affected atoms. All other XRD data were collected using a Rigaku SmartLab diffractometer in Bragg–Brentano mode employing Cu Kα radiation and a D/tex 1-dimensional detector. A nickel filter was used to remove the Cu Kβ radiation component. Data were collected over a 2θ range from 5° to 40° using 0.02° step size at a scan rate of 1°/min. Transmission electron microscopy (TEM) images were taken on a JEOL 2010 EX HREM with an Oxford-Link EDS Gatan digital micrograph equipped with a slow scan CCD camera. Samples were prepared by soaking solar cell devices employing PEDOT:PSS as anode interfacial layers in water and fishing out floating active layers with carbon-coated TEM grids. Optical micrographs were taken on a Carl Zesis Axio Imager 2 microscope at a 400× magnification. High-resolution mass spectrometry (HRMS) was analyzed by using electrospray ionization (ESI) in positive mode on a Waters LCT Premier time-of-flight (TOF) mass spectrometer.

Transient absorption (TA) lifetimes were collected on an Edinburgh Instruments LP920 laser flash photolysis spectrometer. The excitation source consists of a Continuum Surelight II model SLI-10 (Nd:YAG, 10 Hz) with SHG and THG options to generate 532 and 355 nm pump sources. A Surelight SSP (dichroic to separate the 532 and 355 nm signals) is positioned in between the laser and sample to select the pump wavelength. A 450 W ozone free xenon arc lamp is used to generate a microsecond white light probe beam which is arranged in a 90° cross-beam geometry to the incoming laser pulse at the sample. After the sample, the probe beam passes through a spectrograph and is captured by a Hamamatsu R928 PMT (single-wavelength kinetics) or an Andor iStar iCCD camera (TA spectra). Transient data are fit by reconvolution in SurfaceXplorer v4 utilizing a first order multiexponential decay with a fixed instrument response function of 40 ns.

DOI: 10.1021/jacs.7b05801
J. Am. Chem. Soc. 2017, 139, 14109–14119

Scheme 2. Synthetic Scheme

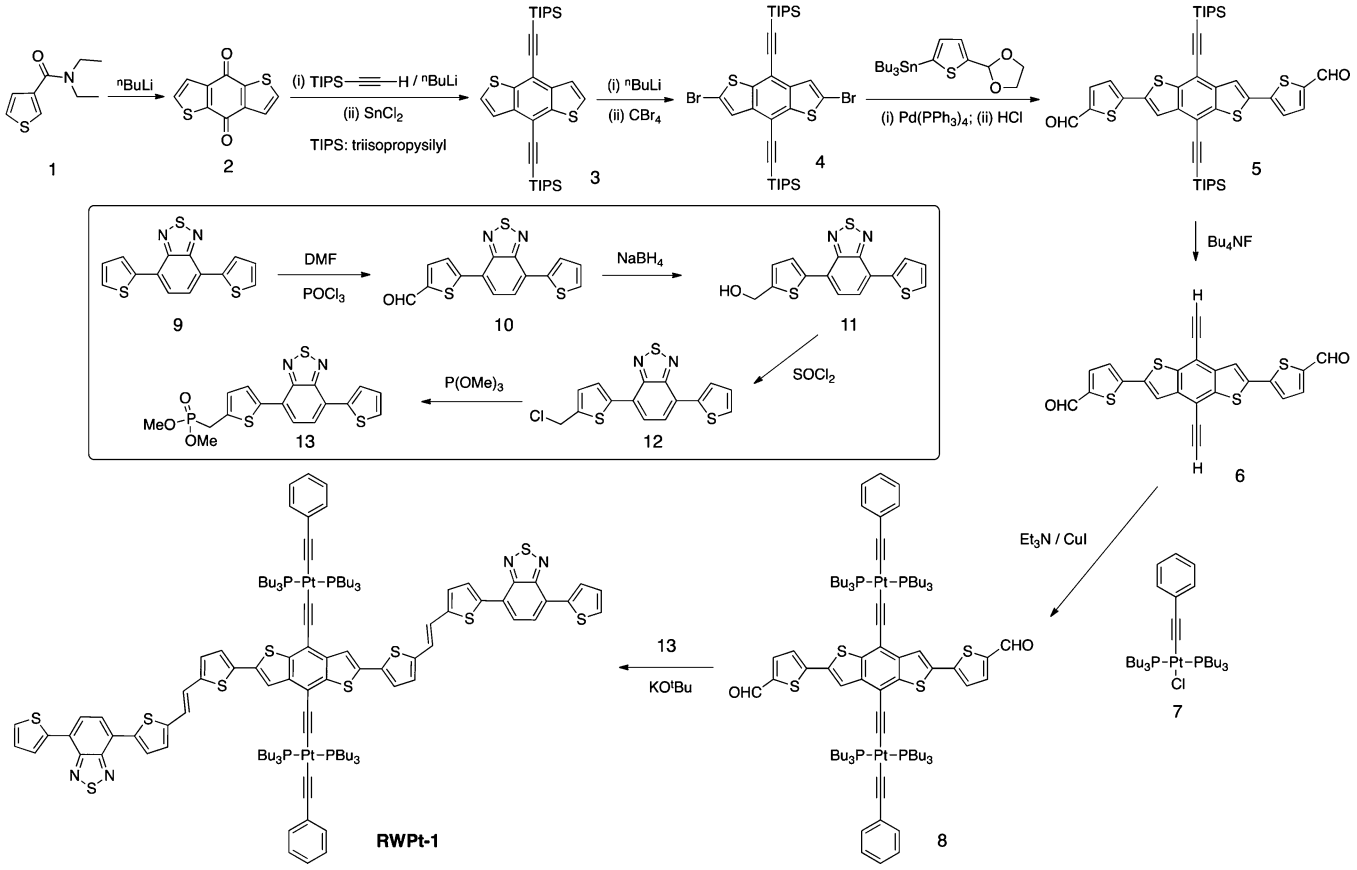

Theoretical calculations are performed on the exact compounds only with the tributylphosphine ligands replaced with trimethylphosphine ligands for computation efficiency. The ground-state geometries are optimized using density functional theory (DFT), and the excited states are calculated with linear response time-dependent DFT (TD-DFT)[17] at the optimized ground-state geometries only. All calculations are performed with the Gaussian 09 package (Rev. D.01)[18] using the hybrid B3LYP functional. The 6-31G* basis set is used for all atoms except for Pt, which has the LANL2DZ basis set for its 5s, 5p, 5d, and 6s valence electrons while the core electrons are replaced by the corresponding pseudopotential.[19] A solvent reaction field simulated by the default polarizable continuum model (PCM) is also employed.[20] We then use the natural transition orbital (NTO) approach[21] to characterize the nature of the lowest singlet and triplet states.

Solar Cell Fabrication and Testing. **RWPt-1**/$PC_{61}BM$ or $PC_{71}BM$ blend solutions were prepared by dissolving **RWPt-1** and $PC_{61}BM$ or $PC_{71}BM$ at predetermined weight ratios in chloroform at a **RWPt-1** concentration of 0.5 wt% and stirred at room temperature for 3−4 h in a nitrogen glovebox (Innovative Technology, model PL-He-2GB, O_2 < 0.5 ppm, H_2O < 0.5 ppm). Solar cell devices were fabricated according to the following procedure: ITO-coated glass substrates (China Shenzhen Southern Glass Display Ltd.; 8 Ω/□) were cleaned by ultrasonication sequentially in detergent water, DI water, acetone, and isopropyl alcohol, each for 15 min. These ITO-coated glasses were further treated by UV-ozone (PSD Series, Novascan) for 60 min before being transferred to a nitrogen glovebox (Innovative Technology, model PL-He-2GB, O_2 < 0.1 ppm, H_2O < 0.1 ppm) for MoO_3 deposition. MoO_3 (10 nm) was deposited using an Angstrom Engineering Amod deposition system at a base vacuum level of <4 × 10^{-7} Torr. The **RWPt-1**/fullerene blend solution was first filtered through a 0.45 μm PTFE filter and spin-coated on top of the MoO_3 layer at 1600 rpm for 30 s. Al (100 nm) was thermally evaporated through patterned shadow masks as cathodes, the size of the active areas is ca. 7.1 mm^2. Current−voltage (I−V) characteristics were measured using a Keithley 2400 source-measuring unit under simulated AM 1.5G irradiation (100 mW/cm^2) generated by a Xe arc-lamp-based Newport 67005 150 W solar simulator equipped with an AM 1.5G filter. The light intensity was calibrated using a Newport thermopile detector (model 818P-010-12) equipped with a Newport 1916-C optical power meter. External quantum efficiency (EQE) values were measured by using a commercial solar cell quantum efficiency measurement system (model QEXL, PV Measurements, Inc., Boulder, CO). The EQE system was calibrated with a Si photodiode certified by the National Renewable Energy Laboratory (NREL).

Synthetic Details. *Compound* ***5***. Compound **4** (1.00 g, 1.42 mmol), tributyl[5-(1,3-dioxolan-2-yl)-2-thienyl]stannane (1.57 g, 3.54 mmol), and $Pd(PPh_3)_4$ (82 mg, 0.071 mmol) were weighed into a pressure-vessel, and 20 mL of toluene was added under argon. The pressure vessel was then sealed and immersed in an oil bath with pre-set temperature at 120 °C for 12 h. After removal of volatile components under vacuum, the crude product mixture was dissolved in THF, and 5 mL of 1 M HCl was added. After being stirred for 1 h, the reaction mixture was extracted with chloroform three times, and the organic phase was combined, washed with water and brine, and finally dried over Na_2SO_4. The crude product was purified by column chromatography on silica gel using hexane/dichloromethane as eluent, and pure compound **5** was obtained by recrystallization from a mixture of $CHCl_3$ and CH_3OH as an orange solid (0.87 g, 80% yield). ^1H NMR (300.13 MHz, $CDCl_3$): δ (ppm) = 9.93 (s, 2H), 7.82 (s, 2H), 7.76 (d, 2H), 7.43 (d, 2H), 1.28 (s, 42H).

Compound ***6***. THF (5 mL) and H_2O (0.1 mL) were added into a Schlenk flask containing compound **5** (64 mg, 0.083 mmol), and the resulting solution was bubbled with N_2 for 15 min, followed by the addition of tetrabutylammonium fluoride trihydrate (TBAF, 65 mg, 0.25 mmol) in 2 mL of THF. The reaction was kept under N_2 for 2 h, and the solvents were evaporated under reduced pressure. The crude product was washed with methanol and collected by filtration.

DOI: 10.1021/jacs.7b05801
J. Am. Chem. Soc. 2017, 139, 14109−14119

Compound **6** was used in the next step without further purification or characterization due to limited solubility in common organic solvents.

*Compound **8**.* To a small vial inside a glovebox were added compound **6** (32 mg, 0.069 mmol), compound **7** (123 mg, 0.167 mmol), and 1 mg of CuI. After 3 mL of anhydrous chloroform and 0.25 mL of anhydrous TEA were injected, the mixture was stirred at room temperature for 12 h. Volatile solvent was removed under reduced pressure, and the crude product was purified by column chromatography using mixtures of hexanes and CH_2Cl_2 as eluents. Compound **8** was further purified by recrystallization from a mixture of $CHCl_3$ and CH_3OH as a red solid (104 mg, 80% yield). ^{1}H NMR (300.13 MHz, $CDCl_3$): δ (ppm) = 9.90 (s, 2H), 7.86 (s, 2H), 7.20 (d, 2H), 7.30 (m, 12H), 2.18 (m, 24H), 1.67 (m, 24H), 1.42 (m, 24H), 0.91 (t, 36H). ^{31}P NMR (121.5 MHz, $CDCl_3$): δ (ppm) = 4.04. ^{13}C NMR (75.48 MHz, $CDCl_3$): δ (ppm) = 182.3, 148.0, 142.3, 139.7, 138.5, 137.1, 135.2, 130.8, 128.9, 127.8, 124.9, 124.8, 123.1, 115.1, 109.6, 107.1, 105.0, 26.5, 24.5, 24.4, 24.3, 24.0, 13.9.

*Compound **12**.* Compound **11** (81 mg, 0.24 mmol) and pyridine (0.13 mL, 1.40 mmol) were dissolved in 10 mL of toluene at 0 °C. Thionyl chloride (0.15 mL, 2.05 mmol) was then added in a dropwise manner at the same temperature. The resulting mixture was stirred at 0 °C for 1 h, followed by stirring at room temperature for 12 h under N_2. The excess thionyl chloride and toluene were removed under reduced pressure. The residue was washed with methanol and isolated as an orange-red solid, which was employed in the next reaction step without further purification (56 mg, 65% yield). ^{1}H NMR (300.13 MHz, $CDCl_3$): δ (ppm) = 8.13 (d, 1H), 7.95 (d, 1H), 7.87 (d, 2H), 7.86 (d, 2H), 7.48 (d, 2H), 7.18 (m, 2H) 4.87 (s, 2H). ^{13}C NMR (75.48 MHz, $CDCl_3$): δ (ppm) = 152.4, 152.3, 141.2, 140.6, 139.1, 128.5, 128.0, 127.6, 127.0, 126.9, 126.2, 125.6, 125.5, 125.3, 40.6.

*Compound **13**.* Compound **12** (90 mg, 0.26 mmol) was mixed with 3 mL of $P(OMe)_3$, and the resulting mixture was stirred at 135 °C for 12 h under argon. After the mixture cooled to room temperature, volatile components were removed under reduced pressure, and compound **13** was purified by column chromatography (hexanes and CH_2Cl_2) as a dark red solid (37 mg, 34% yield). ^{1}H NMR (300.13 MHz, $CDCl_3$): δ (ppm) = 8.00 (d, 1H), 7.86 (d, 1H), 7.65 (d, 1H), 7.63 (d, 1H), 7.40 (d, 1H), 7.13 (dd, 1H), 7.02 (dd, 1H), 3.79 (d, 6H), 3.45 (d, 2H). ^{31}P NMR (121.5 MHz, $CDCl_3$): δ (ppm) = 26.9. ^{13}C NMR (75.48 MHz, $CDCl_3$): δ (ppm) = 152.1, 152.0, 139.0, 138.6, 138.5, 133.5, 133.4, 128.3, 128.2, 127.7, 127.4, 127.3, 127.2, 126.5, 125.4, 125.2, 124.9, 53.0, 52.9, 28.1, 26.2.

RWPt-1. Compound **13** (180 mg, 0.426 mmol) and compound **8** (285 mg, 0.153 mmol) were dissolved in 30 mL of THF inside a glovebox. Potassium *tert*-butoxide (69 mg, 0.613 mmol) in 5 mL of THF was then added in a dropwise manner to the solution with stirring at room temperature. The resulting mixture immediately turned from red-orange to dark purple. The reaction mixture was stirred at room temperature for 12 h before the solvents were removed under reduced pressure. The crude product was purified by column chromatography (hexanes/CH_2Cl_2), and **RWPt-1** was further purified by recrystallization from a mixture of $CHCl_3$ and CH_3OH as a dark solid (300 mg, 75% yield). ^{1}H NMR (300.13 MHz, $CDCl_3$): δ (ppm) = 8.14 (dd, 2H), 8.07 (d, 2H), 7.90 (dd, 4H), 7.68 (s, 2H), 7.48 (dd, 2H), 7.32 (m, 4H), 7.15 (m, 18H), 2.21 (m, 24H), 1.70 (m, 24H), 1.48 (m, 24H), 0.95 (t, 36H). ^{31}P NMR (121.5 MHz, $CDCl_3$): δ (ppm) = 4.00. ^{13}C NMR (75.48 MHz, $CDCl_3$): δ (ppm) = 152.7, 152.5, 143.7, 141.8, 139.6, 138.8, 138.4, 138.2, 137.8, 135.9, 130.9, 129.0, 128.3, 128.0, 127.8, 127.6, 127.5, 126.9, 125.9, 125.8, 125.6, 125.4, 124.9, 122.0, 121.3, 120.5, 114.2, 109.6, 107.9, 107.7, 107.5, 105.3, 26.5, 24.5, 24.4, 24.3, 24.2, 24.0, 13.9. HRMS (ESI): $C_{118}H_{142}N_4P_4Pt_2S_{10}$, calcd, 2448.6688 for $[M^+]$; found, 2448.6716 for $[M^+]$.

3. RESULTS AND DISCUSSION

The detailed synthetic procedure of **RWPt-1** is shown in Scheme 2, which adopts a convergent route by separately preparing the Pt-bisacetylide benzenedithiophene (BDT) core **8** and π-conjugated arms **13** first. The final step involves a Wittig–Horner-type condensation reaction between compound **8** and 2 equiv of **13** in the presence of a strong base, KO^{t}Bu. Compared with the structure of **RWPt-2**, the roller in **RWPt-1** is longer by one thiophene unit and one double bond on each side of the Pt-bisacetylide BDT core. The reason for not using fully aromatic moieties in constructing **RWPt-1** is that we found unidentifiable byproducts during the last step of synthesis for **RWPt-2**, which involved Pd[0]-catalyzed Stille cross-coupling reactions and led to poor product yield after repetitive purification steps. There were always a few small side peaks in the ^{31}P NMR spectra of **RWPt-2**, although ^{1}H, ^{13}C, and ^{19}F NMR showed no signs of impurities. After several control experiments, we found that addition of Pd[0] complexes alone could induce the formation of the same set of ^{31}P NMR impurity signals. As a result, we decided to apply the Pd-free Wittig–Horner reaction for the last step during the synthesis of **RWPt-1**. On the other hand, the fluorinated benzothiadiazole (F-BTD) units in **RWPt-2** were found to be incompatible with the strong base used in Wittig–Horner reaction, which involved substitution of the fluorine atoms with the O^{t}Bu groups. Thus, non-fluorinated BTD units were used in the construction of **RWPt-1**. As expected, **RWPt-1** was obtained in 75% yield after column chromatography, and recrystallization to give a dark crystalline solid that melts at ca. 88 °C as estimated by DSC (Supporting Information (SI), Figure S1) and fully characterized by NMR spectroscopy and HRMS. In addition, the ^{31}P NMR spectrum (SI) shows a single peak at 4.00 ppm with two Pt satellites having $J_{Pt-P} \approx 2349$ Hz, confirming the stability of Pt-bisacetylide complexes under the strongly basic conditions applied.

We were able to obtain good-quality single crystals of **RWPt-1** for detailed X-ray analysis, and the representative structure and packing diagrams are shown in Figure 1. **RWPt-1** crystallizes into a triclinic crystal system with space group $P\bar{1}$ (a = 11.6264(18) Å, b = 16.274(2) Å, c = 17.868(3) Å, α = 64.226(5)°, β = 82.203(5)°, γ = 78.775(5)°). The multiple aromatic rings constituting the roller are largely coplanar in geometry, except noticeable twists between the S1-thiophene ring and S2-thiophene ring, and between the S2-thiophene ring and S3-thiophene ring, with torsional angles of ca. 11.3° and ca. 17.7°, respectively. The larger twist of the later is likely caused by the more flexible double bond between the aromatic units, although insertion of double bonds generally eliminates steric hindrance between aromatic groups. The four tributylphosphine ligands are situated above and below the aromatic plane, with all four Pt–P bonds approximately perpendicular to the BDT core. The two terminal phenyl rings are approximately coplanar, both of which are twisted at ca. 49° relative to the BDT core. The packing diagrams viewed along the b-axis (Figure 1B) and c-axis (Figure 1C) unambiguously confirm the proposed slip-stack packing motif of **RWPt-1**. As Figure 1B shows, the right arm of the **RWPt-1** molecule on the left overlaps with the left arm of the molecule adjacent to the right. The electron-deficient BTD rings preferentially eclipse with the thiophene rings next to the BDT cores, and the terminal thiophene rings overlap with the respective thiophene unit of BDT core of the next molecule. The remaining thiophene rings and double bonds are thus offset between the stacked molecules. When viewed from the side (Figure 1C), the vertical distance between the overlapping arms is ca. 3.6–3.9 Å, which is characteristic of typical π–π stacking distances among aromatic molecules.[22] Single crystals of **RWPt-3** were also obtained as shown in Figure S2. However, no slip-stacking can

DOI: 10.1021/jacs.7b05801
J. Am. Chem. Soc. 2017, 139, 14109–14119

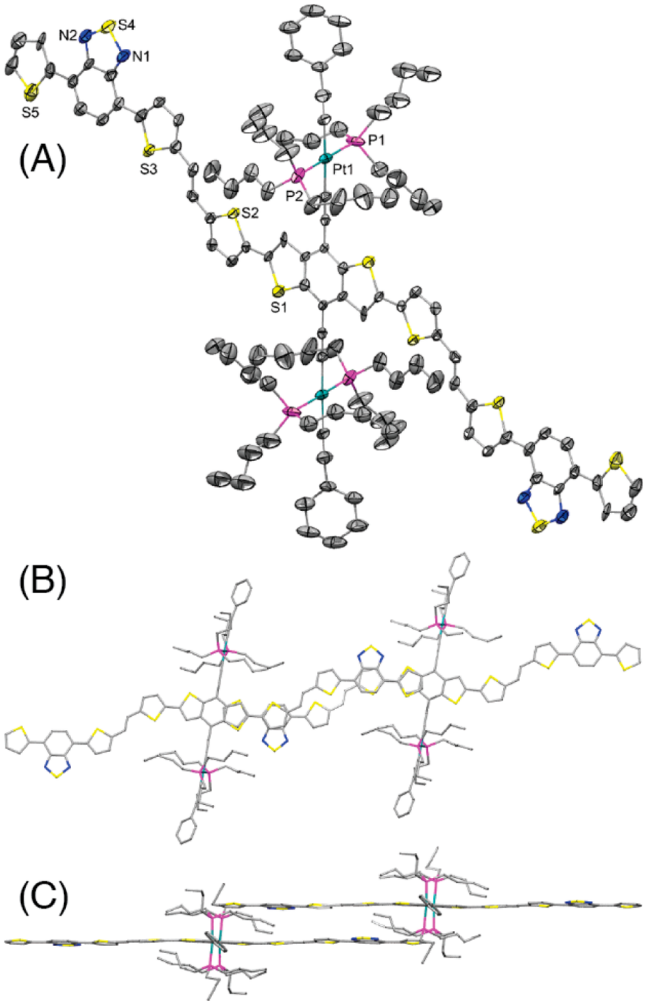

Figure 1. (A) Crystal structure of **RWPt-1**; thermal ellipsoids are drawn at 50% probability. Hydrogen atoms and the co-crystallized chlorobenzene solvent molecules (disordered) have been omitted for clarity. Three butyl chains are disordered over two positions; only the major position is show. Packing diagrams are also shown as viewed along (B) the *b*-axis and (C) the *c*-axis.

be observed since the length of the conjugated roller is comparable with the sizes of the tributylphosphine ligands, which results in the distance among adjacent π systems being more than 7 Å, too large for efficient electronic communication. The lack of efficient $\pi-\pi$ stacking was also previously observed in a roller-wheel-type Pt-containing single-crystal molecule reported by Schanze et al., which features triphenylamine-terminated phenylenevinylene as the conjugated roller.[13] Thus, roller lengths significantly longer than the spread of tributylphosphine ligands are prerequisites for slip-stacked packing motifs in these roller-wheel Pt-containing molecules. Furthermore, XRD patterns (Figure S3A) of thin films of **RWPt-1** drop-cast onto glass substrates display relatively sharp scattering signals that can all be properly indexed according to simulated powder patterns from single-crystal data (Figure S3B), suggesting similar slip-stacking motifs in the thin films. On the other hand, XRD of **RWPt-2** (Figure S3C) displays fewer and relatively broader signals, suggesting less crystallinity when compared with **RWPt-1**. The peak at 2θ of 23.2° corresponds to a *d*-spacing of ca. 3.8 Å, indicating the existence of slip-stacking between adjacent **RWPt-2** molecules.

Electronic properties of these roller-wheel compounds are studied by steady-state absorption and emission spectroscopy as shown in Figure 2A,B for **RWPt-1**, in Figure S4 for **RWPt-2**,

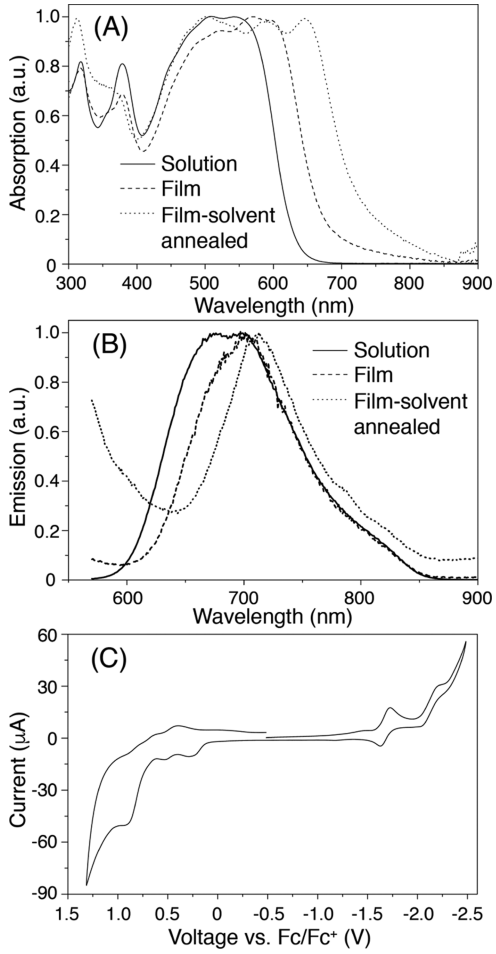

Figure 2. UV−vis absorption (A) and emission (B) profiles of **RWPt-1** in chloroform solutions (10^{-5} M, solid lines), as thin film drop-cast onto glass substrates (dashed lines), and as thin films after solvent annealing using chloroform for 2 min (dotted lines). (C) Cyclic voltammogram (CV) of **RWPt-1** in CH_2Cl_2 (1 mM) with Bu_4NPF_6 as supporting electrolyte (0.1 M). The potential is calibrated externally to the ferrocene (Fc) redox couple (4.80 V below vacuum).

and in Figure S5 for **RWPt-3**. In dilute solutions, **RWPt-1** displays multiple strong absorption peaks at ca. 318, 378, and 400−600 nm, the onset of which is estimated to be ca. 630 nm, leading to a solution optical bandgap of ca. 1.97 eV. Similarly, **RWPt-2** shows multiple resolved absorption peaks in solutions at ca. 322, 363, 441, 488, and 555 nm, and its optical bandgap is estimated to be ca. 1.94 eV. Although the roller and thus conjugation length in **RWPt-1** is longer than that in **RWPt-2**, both compounds have very close optical bandgaps in solutions. Presumably, the presence of double bonds increases flexibility and decreases coplanarity of the roller in **RWPt-1** in solutions, and the presence of strongly electron-withdrawing F atoms on the BTD units increases the strengths of intramolecular charge transfer (ICT) interactions in **RWPt-2**. On the other hand, **RWPt-3** is a wide-bandgap material and also displays multiple absorption peaks at ca. 317, 355, 392, 436, and 464 nm and an optical bandgap of ca. 2.53 eV. This is easily understood since the roller length in **RWPt-3** is significantly shorter than those in

DOI: 10.1021/jacs.7b05801
J. Am. Chem. Soc. 2017, 139, 14109−14119

the other two compounds and there are no ICT transitions. Noticeably, the absorption profiles below 500 nm for all three compounds bear significant similarity, which indicates that the higher energy electronic transitions likely originate from the Pt-BDT core, while the additional lower energy transitions observed in **RWPt-1** and **RWPt-2** are mainly due to ICT transitions. When cast into thin films, the absorption profiles of both **RWPt-1** and **RWPt-2** experience large bathochromic shifts, with new lowest energy absorption peaks at ca. 600 and 640 nm, respectively. The solid-state optical bandgaps are then estimated to be ca. 1.85 and 1.80 eV, respectively for **RWPt-1** and **RWPt-2**. In contrast, a very small red-shift in the lowest energy transition peaks from 464 to 470 nm is observed in **RWPt-3** from solutions to thin films. These observations confirm the better $\pi-\pi$ interactions in **RWPt-1** and **RWPt-2** due to the longer roller lengths and slip-stacked geometries, as well as the lack thereof in **RWPt-3**. Interestingly, when the thin films of **RWPt-1** were exposed to chloroform vapor, the absorption profile exhibits further red-shift, and a new peak emerges at ca. 650 nm, leading to a much reduced bandgap of ca. 1.72 eV. However, the same solvent vapor annealing treatment did not cause noticeable changes in the absorption of **RWPt-2**. We ascribe such differences to the flexibility of double bonds. In as-cast films, the **RWPt-1** molecules may be at kinetically trapped states having less planar aromatic roller due to the large rotational freedom around the double bonds. Solvent annealing then increases the free volumes and local movement of the molecular chains, resulting in the more thermodynamically stable state, i.e., the more planar and slip-stacked geometry as revealed by the crystal structure. Both **RWPt-1** and **RWPt-2** display weak fluorescence in solutions peaked at ca. 675/698 and 700 nm, respectively, and the quantum efficiencies are both below 1% using quinine bisulfate as the standard. **RWPt-3** displays both fluorescence and phosphorescence in solution at ca. 488 and 705 nm, respectively. The 705 nm peak is assigned to phosphorescence because it can only be observed in the absence of oxygen that is known to effectively quench triplet states. From the energy difference between fluorescence and phosphorescence peaks, a singlet−triplet energy gap in **RWPt-3**, ΔE_{ST} is estimated at ca. 0.78 eV. If we apply this ΔE_{ST} value to **RWPt-1** and **RWPt-2**, we will obtain the lowest triplet energy E_{T1} = 1.19 and 1.16 eV, respectively. These relatively low E_{T1} energy levels likely explain the absence of phosphorescence in these low bandgap roller-wheel compounds, according to the energy gap law.[23] The emission profile of **RWPt-1** thin films is very similar to that of solutions, except the relative intensities between the 675 and 698 nm peaks with intensity of the latter being relatively enhanced. After solvent vapor annealing, the emission peak slightly red-shifts to 713 nm, consistent with the observed absorption behavior. On the other hand, the emission peak of **RWPt-2** thin films experiences a small blue shift to ca. 680 nm, suggesting H-type aggregation of the chromophores.[24] The emission profile of **RWPt-3** thin films displays a new broad emission peak at ca. 575 nm, the origin of which is currently unknown.

The highest occupied molecular orbital (HOMO) and lowest unoccupied molecular orbital (LUMO) energies of **RWPt-1** were estimated by using cyclic voltammetry (CV) in solutions as shown in Figure 2C. Three irreversible oxidation waves and two quasi-reversible reduction waves can be observed. From the onsets of the first oxidation and reduction peaks using ferrocene redox couple as an external standard (−4.8 eV), the HOMO and LUMO levels of **RWPt-1** are respectively estimated at −4.9 and −3.2 eV. The HOMO and LUMO energy levels of **RWPt-2** in solutions were estimated respectively at −5.0 and −3.2 eV, leading to an electrochemical bandgap similar to that of **RWPt-1**, consistent with solution absorption observations.

Due to the lack of phosphorescence in **RWPt-1** and **RWPt-2**, we performed nanosecond TA spectroscopic measurements to study the triplet states in these molecules as shown in Figure 3AB. The TA data for **RWPt-3** are presented in Figure 3C. The TA spectra of **RWPt-1** exhibit two bleach (negative) features from 350 to 600 nm and an excited-state absorption (positive) feature from 600 to 800 nm. The two negative features are ascribed to loss of ground state, because the shapes of these features strongly mirror the absorption spectra in Figure 2A. The long wavelength excited-state absorption is ascribed to the triplet state of **RWPt-1** based on similarities to the TA spectra of previously reported for closely related Pt-bisacetylide containing molecular species,[5f,i,7b,25] as well as from its relatively long excited-state lifetime on the microsecond time scale (see below). Single-wavelength kinetics collected at 780 and 550 nm are fit with monoexponential decays to yield respective constants of 5.4 ± 0.1 and 4.9 ± 0 μs, which is in accord with the 5.0 ± 0.1 μs lifetime obtained from global fitting analysis. These wavelengths correspond to the excited-state absorption and ground-state bleach regions, respectively, indicating re-formation of the **RWPt-1** ground state. The presence of an isosbestic point (∼600 nm) and agreement in the lifetime suggest no intervening state. Similarly for **RWPt-2**, the TA spectra display four negative peaks from 340 to 600 nm and a broad excited-state absorption from 600 to 850 nm, respectively assigned to ground-state bleach and triplet excited-state absorption. In contrast to **RWPt-1**, single-wavelength kinetics at 700 nm (excited-state absorption) and 500 nm (ground-state bleach) can only be fit with biexponential decays (at both wavelengths) that retrieve time constants of 7.5 ± 0.4 and 16.3 ± 0.4 μs, respectively (global fitting analysis reveals 6.1 ± 0.4 and 14.1 ± 0.2 μs). Additionally for **RWPt-3**, biexponential decay (at 600 and 700 nm) with excited-state lifetimes of 22 ± 5 and 70 ± 7 μs were found (global fitting analysis reveals 22.5 ± 0.1 and 63.5 ± 0.1 μs). The 70 μs lifetime is due to compound decomposition (30% contribution in fit), as the ΔOD signal never returned to zero at long time delays (hundreds of microseconds). Importantly, we do not see evidence for a 70 μs time constant in either **RWPt-1** or **RWPt-2**.

Assignment of these lifetimes is best understood through comparison of the three complexes and nicely supported by the computational data (see below). The 22 μs time constant in **RWPt-3** represents the excited-state lifetime of the structural core of **RWPt-1** and **RWPt-2**, and contains both Pt→BDT and BDT $\pi\rightarrow\pi^*$ character. In contrast, the 5 μs time constant in **RWPt-1** represents ground-state recovery that does not involve the **RWPt-3** structural core. We propose that the origin of these spectral dynamics in **RWPt-1** is localized on the benzodithiadiazole (BTD) moieties on the periphery. For **RWPt-2**, there is good agreement of the observed lifetimes of ∼7 and ∼16 μs with the lifetimes of **RWPt-1** (5 μs) and **RWPt-3** (20 μs) to suggest the presence of two non-interacting triplet states, one on the Pt-BDT core and one on the BTD peripheral structures. We are presently investigating the femtosecond to sub-nanosecond dynamics of the excited states in this series of

DOI: 10.1021/jacs.7b05801
J. Am. Chem. Soc. 2017, 139, 14109−14119

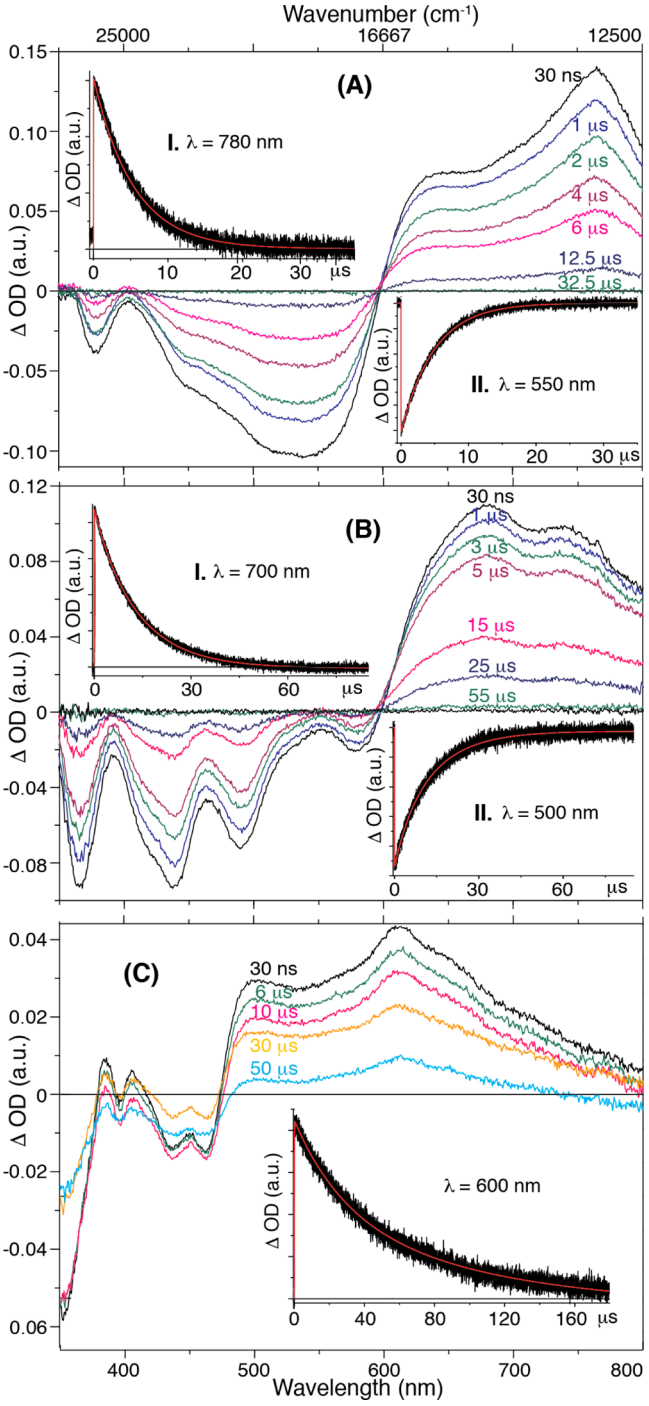

Figure 3. Transient absorption spectra of (A) **RWPt-1**, (B) **RWPt-2**, and (C) **RWPt-3**, collected in chlorobenzene solution (10^{-5} M), excited at 532 nm with a nanosecond pulse from a SHG Continuum Surelight Nd:YAG laser at 1 Hz. The first transient spectrum was collected at 30 ns in order to omit effects from the excitation pulse. Insets: Single-wavelength kinetic traces (black) and monoexponential fits (red).

complexes to learn more about these complicated chromophores.

In order to further understand the observed photophysical phenomena, we have performed DFT studies on these roller-wheel compounds, and the results are summarized in Figure 4. All non-essential side chains are replaced with methyl groups for computation efficiency, and the ground-state geometries are optimized using DFT, while the excited states are calculated with linear response TD-DFT[17] at the optimized ground-state geometries only. The calculations were performed by using the Gaussian 09 package (Rev. D.01)[18] applying the hybrid B3LYP functional. The 6-31G* basis set is used for all atoms except for Pt, for which the LANL2DZ basis set is applied for its 5s, 5p, 5d, and 6s valence electrons with the core electrons replaced by the corresponding pseudopotential.[19] We also employ a solvent reaction field simulated by the default PCM.[20] The NTO approach[26] is then utilized to characterize the nature of the lowest singlet and triplet states, and only the dominating representations are shown.

All three compounds are found to possess two bright singlet states. The S1-state energies for **RWPt-1** and **RWPt-2** are estimated respectively at ca. 1.59 and 1.55 eV, slightly lower than those observed in solution absorption spectroscopy but consistent with the measured similar optical bandgaps. From the NTOs that approximately represent the hole and electron in the transitions, both S1 states have clear $\pi-\pi^*$ and ICT characters mixed with metal-to-ligand charge-transfer (MLCT) transitions, as expected from the electron-rich Pt-BDT core and electron-poor BTD arms, as well as the hole density delocalized into the Pt-bisacetylide moieties. The existence of such ICT states likely explains the underestimated S1 energies, considering the previously shown difficulties of TD-DFT calculations with charge-transfer states.[21] Accordingly, the S1 state of **RWPt-3** is largely of $\pi-\pi^*$ and MLCT characters, and the calculated energy at 2.53 eV matches very well with the optical bandgap. The T1-state energies for **RWPt-1**, **RWPt-2**, and **RWPt-3** are estimated to be ca. 1.06, 1.12, and 1.67 eV, respectively, all of which are very close to the values calculated from the optical bandgaps and ΔE_{ST} of **RWPt-3**. The low-lying T1 states of both **RWPt-1** and **RWPt-2** may pose potential problems for electron transfer and charge separations in OSC devices as discussed below. From TA spectroscopy, seemingly two triplet decay time constants, one shorter and the other longer, are found in these three compounds, with **RWPt-1** giving only the shorter constant and **RWPt-3** giving only the longer constant, while both constants are observed for **RWPt-2**. We can safely assign the longer time constant to the Pt-bisacetylide BDT core, i.e., the T1 state of **RWPt-3** having largely $\pi-\pi^*$ character. The T3 state of **RWPt-1** bears significant resemblance in hole/electron density maps as well as in energy with those of the T1 state of **RWPt-3**, but the similarity with its T1 state can lead to fast internal conversion processes from T3 to T1 and the absence of an observed long lifetime constant. On the other hand, the T3 state of **RWPt-2** bears significant dissimilarity with its T1 and T2 states, and is likely responsible for the longer decay lifetime observed. As for the shorter time constant, we believe it originates from the triplet states possessing ICT characters, since it is observed in both **RWPt-1** and **RWPt-2** molecules, but not in **RWPt-3**.

One of the key characteristics for organic electronic devices is the material's charge mobility, and we have thus performed hole mobility measurements on **RWPt-1**, **RWPt-2**, and **RWPt-3** by using space charge limited current method,[27] in hole-selective device geometries (ITO/MoO_3/organic/MoO_3/Al). The hole mobilities of **RWPt-1** are estimated to be 5.1×10^{-5} cm^2 V^{-1} s^{-1} for as-cast films and 2.0×10^{-4} cm^2 V^{-1} s^{-1} for thin films after solvent vapor annealing, while the hole mobilities for **RWPt-2** and **RWPt-3** are estimated at 1.5×10^{-5} and 1.6×10^{-6} cm^2 V^{-1} s^{-1}, respectively. These data correlate very well with the differences in crystallinity and $\pi-\pi$ stacking motifs in

DOI: 10.1021/jacs.7b05801
J. Am. Chem. Soc. 2017, 139, 14109−14119

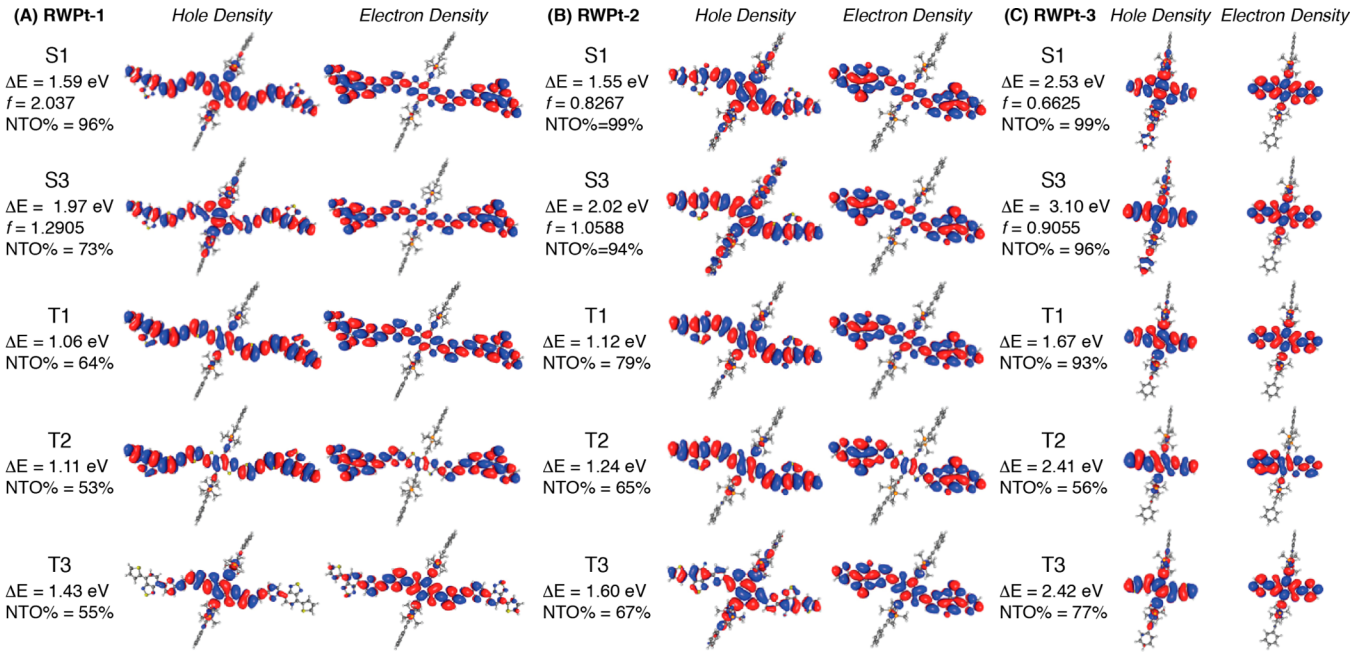

Figure 4. Low-lying bright singlet states and triplet states of (A) **RWPt-1**, (B) **RWPt-2**, and (C) **RWPt-3** calculated by density functional theory (DFT). ΔE is transition energy; f is oscillator strength; NTO is natural transition orbital.

these compounds and confirm the effectiveness of slip-stacking in promoting intermolecular electronic communication.

Bulk heterojunction OSC devices with conventional structures, ITO glass/MoO_3 (10 nm)/organic (100 nm)/Al (10 nm), were fabricated employing these roller-wheel compounds and fullerene derivatives. Devices using **RWPt-3** gave almost zero efficiency under various fabrication conditions (Table 1), understandably caused by its relatively wide bandgap, inefficient intermolecular electronic communications, and low charge mobility that lead to large series resistance and recombination-induced V_{OC} loss. Thus, we will only focus on devices applying **RWPt-1** and **RWPt-2** in the following discussions. Devices were first constructed by using $PC_{61}BM$ as the electron acceptor and optimized by varying the fabrication conditions including spin-coating speed, weight ratios, concentrations, and annealing conditions; $PC_{71}BM$ was then applied using the optimized condition for $PC_{61}BM$. The optimization details for **RWPt-1** are summarized in Table S1, and those for **RWPt-2** were reported previously,[8] while optimized device parameters applying $PC_{71}BM$ are listed in Table 1.

Table 1. Optical and Electronic Properties and Organic Solar Cell Performances of RWPt-1, RWPt-2, and RWPt-3

	RWPt-1	RWPt-2	RWPt-3
E_g (eV)[a]	1.97 (1.72)[b]	1.94 (1.80)	2.53 (2.53)
μ_{hole} (cm^2 V^{-1} s^{-1})[c]	5.1×10^{-5} (2.0×10^{-4})[b]	1.5×10^{-5}	1.6×10^{-6}
J_{SC} (mA/cm^2)[d]	11.2 ± 1.0 (12.9)[h]	11.9 ± 1.5 (14.4)[i]	0.06[j]
V_{OC} (V)[e]	0.79 ± 0.00 (0.80)[h]	0.82 ± 0.03 (0.85)[i]	0.35[j]
FF (%)[f]	36 ± 2 (39)[h]	57 ± 5 (63)[i]	50[j]
PCE (%)[g]	3.2 ± 0.3 (3.9)[h]	5.6 ± 0.3 (5.9)[i]	0.01[j]
R_S (Ω cm^2)[k]	32.1 ± 10.3	5.6 ± 1.6	2410 ± 270
R_{SH} (Ω cm^2)[l]	172 ± 33	880 ± 520	5480 ± 1670

[a]Optical bandgap in solution; thin-film data are presented in parentheses. [b]Data for thin films after solvent annealing. [c]Hole mobility. [d]Short-circuit current. [e]Open-circuit voltage. [f]Fill factor. [g]Power conversion efficiency. [h]As-cast devices using **RWPt-1**/$PC_{71}BM$ weight ratio of 1/2. [i]Devices employing **RWPt-2**/$PC_{71}BM$ at a weight ratio of 1/0.8, with solvent annealing in chloroform for 2 min. [j]As-cast devices using **RWPt-3**/$PC_{61}BM$ weight ratio of 1/1. [k]Series resistance. [l]Shunt resistance. Average are calculated from at least five devices, and best values are given in parentheses.

RWPt-1 and **RWPt-2** gave OSC PCEs up to 3.9% and 5.9%, respectively, and to the best of our knowledge, **RWPt-2** has out-performed all existing Pt-containing polymers and SMs in OSC devices. Devices applying both compounds display comparable short-circuit current (J_{SC}) and open-circuit voltage (V_{OC}) values, likely due to the similar absorption profiles and bandgaps, as well as the HOMO energy levels. The major difference is in the fill factor (FF) values, with the highest FF for **RWPt-1** devices being 39%, while that for **RWPt-2** devices up to 63%. The low FF for **RWPt-1** devices is clearly seen in the current density−voltage (J−V) plot in Figure 5A, in which a much larger current increase under negative bias is observed in the J−V curve for **RWPt-1** than that for **RWPt-2**, effectively leading to a smaller shunt resistance and FF. Such difference is also reflected in external quantum efficiency (EQE) measurements. The EQE profiles of both **RWPt-1** (Figure 5A, inset) and **RWPt-2** (Figure S6) display photoresponses from 300 to 700 nm, matching well with the device absorption spectra, while the EQE values for **RWPt-2** devices are constantly higher than those for **RWPt-1** devices across the entire response range.

It is noticed that the best performance for **RWPt-1** devices was obtained only in as-cast blend films, and solvent vapor annealing or thermal annealing both led to gradually decreasing J_{SC}, FF, and thus PCE values. On the other hand, the best performance of **RWPt-2** devices was achieved after solvent vapor annealing for 2 min. It has been well-established that in OSCs the J_{SC} and FF are closely related to blend morphologies,

DOI: 10.1021/jacs.7b05801
J. Am. Chem. Soc. 2017, 139, 14109−14119

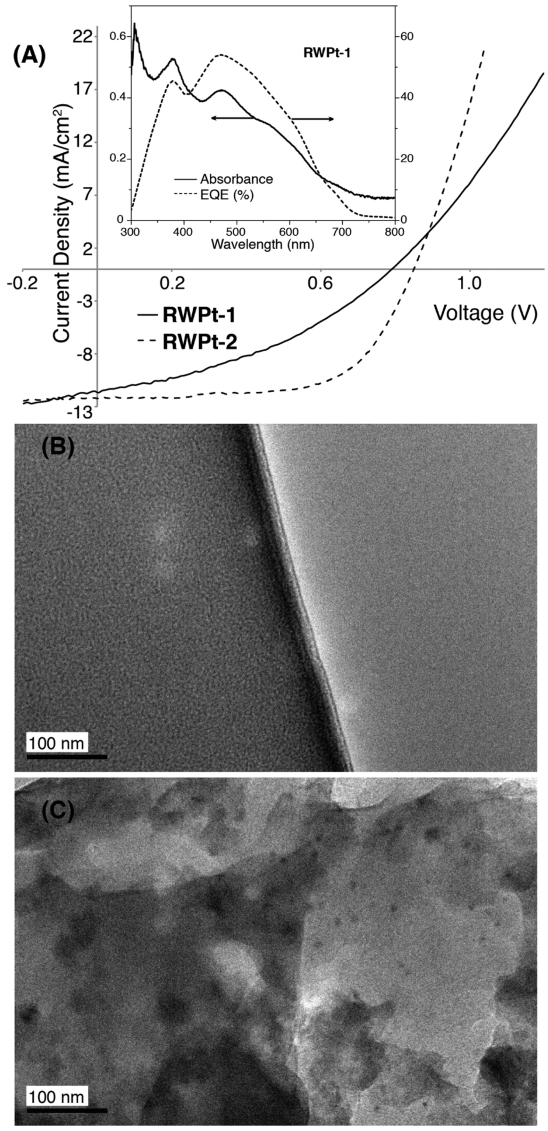

Figure 5. (A) Current density−voltage (J−V) curves of the best performing solar cell devices employing **RWPt-1** (solid line) and **RWPt-2** (dashed line). Inset: absorption (solid line) and external quantum efficiency (EQE) (dashed line) profiles of the best performing **RWPt-1** device. (B) Transmission electron microscopy (TEM) image of the as-cast active layer of the best performing **RWPt-1** device. (C) TEM image of the active layer of the best performing **RWPt-1** device after solvent vapor annealing for 2 min.

for which a bicontinuous donor−acceptor network with domain sizes comparable to the exciton diffusion lengths is crucial to achieve high performance. We have demonstrated that solvent vapor annealing for 2 min led to a bicontinuous network with domain sizes on the order of 5−10 nm in **RWPt-2** devices, although extended annealing led to macrophase separation and device deterioration.[8] We thus studied the active layer morphologies of **RWPt-1** devices in detail by using TEM and OM, and representative images are shown in Figure 5B,C and Figure S7, respectively. The TEM image of as-cast blend films of **RWPt-1** and $PC_{71}BM$ (Figure 5B) displays smooth morphology with finely interpenetrated domains of less than 5 nm in size. Upon chloroform vapor annealing for 2 min (Figure 5C), large aggregates having sizes ranging from tens to 100 nm appear. These darker regions are presumably crystallites of **RWPt-1** due to the presence of heavy metal Pt. The OM image of the same blend layer before solvent vapor annealing (Figure S6A) display featureless morphology, but after annealing for 2 min, micrometer-sized aggregates are clearly observed (Figure S6B).

We thus rationalize the observed device behaviors for **RWPt-1** and **RWPt-2** as follows. From optical and theoretical studies, the T1-state energy levels of both compounds are estimated to be ca. −3.9 eV which is very close to the LUMO energy levels of fullerene derivatives at ca. −4.0 eV. Thus, the applied fullerene derivatives are unlikely to induce efficient electron transfer from the triplet state of either **RWPt-1** or **RWPt-2**. The lack of electron transfer is further suggested by the identical TA spectra of both **RWPt-1** and **RWPt-2** solutions with (up to 10 equiv) or without the presence of fullerenes. As a result, photocurrents of both devices should mainly originate from charge separation of singlet states. Due to the presence of heavy Pt atoms and efficient ISC events, the domain sizes of the donors need to be small enough in order for the singlet excitons to be captured by nearby fullerenes before being converted to triplets. Caused by the high crystallinity of **RWPt-1**, the as-cast blend films already possessed certain phase separation as well as molecularly mixed regions, as revealed by TEM analysis. Such morphology helped capturing the singlet states leading to decent PCEs but was not ideal as reflected by the relatively low FF values. Annealing possibly leads to fast crystallization of **RWPt-1** and domain sizes significantly larger than the singlet diffusion lengths, resulting in the quick drop in device efficiencies. On the other hand, **RWPt-2** has been shown to possess less crystallinity due to the shorter roller lengths, which provides a wider window for optimization and led to the optimized morphologies after solvent vapor annealing as well as superior device performances.

4. CONCLUSIONS

In summary, we have proposed a new design concept, i.e., the "roller-wheel" geometry, in Pt-bisacetylide containing small molecules, and have prepared three such molecules possessing different roller characteristics. By such design, molecules with extended "rollers" expectedly adopt a "slip-stack" packing motif in the solid state, leading to high crystallinity and charge mobility. Transient absorption measurements and theoretical calculations reveal long-lived triplet states in these molecules having both π−π^* and intramolecular charge transfer characters. OSC devices employing the low bandgap compounds **RWPt-1** and **RWPt-2** showed PCEs among the highest reported to date for Pt-containing polymers and SMs, which are however very sensitive to optimization conditions and device morphologies. The underlying reason is that the energy of the lowest triplet excited states is too small for efficient electron transfer to fullerene acceptors, and only short-lived singlet excited states can lead to charge separation in these devices. We are currently investigating such early dynamics, including charge separation from the singlet and/or triplet states and ISC events, in the blend devices with different electron acceptors, including fullerene derivatives and emerging non-fullerene small molecules,[28] having varied LUMO energy levels by using ultrafast spectroscopy, which will be reported in a separate account. Another possibility is to design molecules with small ΔE_{ST} that can lead to higher T1 energy levels while maintaining low optical bandgaps, such as borrowing the design rules from molecules possessing thermally activated delayed fluorescence.[29] Our roller-wheel designs can be further

DOI: 10.1021/jacs.7b05801
J. Am. Chem. Soc. 2017, 139, 14109−14119

extended to polymeric structures to form poly(roller-wheel)s that can potentially lead to better film-forming ability and blend morphologies, which is currently under investigation.

■ ASSOCIATED CONTENT

Supporting Information

The Supporting Information is available free of charge on the ACS Publications website at DOI: 10.1021/jacs.7b05801.

Single-crystal structure of **RWPt-1** (CIF)
Single-crystal structure of **RWPt-3** (CIF)
DSC histograms of **RWPt-1**, single-crystal structure and packing of **RWPt-3**, film XRD profiles of **RWPt-1** and **RWPt-2**, absorption and emission spectra of **RWPt-2** and **RWPt-3**, EQE and absorption profiles of **RWPt-2** devices, optical micrographs of OSC devices applying **RWPt-1**, details for device optimization of **RWPt-1**, and NMR spectra, including Figures S1−S7 and Table S1 (PDF)

■ AUTHOR INFORMATION

Corresponding Authors

*jrack@unm.edu
*qinwu@bnl.gov
*yangqin@unm.edu

ORCID

Jeffrey J. Rack: 0000-0001-6121-879X
Qin Wu: 0000-0001-6350-6672
Yang Qin: 0000-0002-5764-8137

Present Address

†D.A.D.: Department of Chemistry, Brandeis University, 415 South St., Waltham, MA 02453

Notes

The authors declare no competing financial interest.

■ ACKNOWLEDGMENTS

The authors would like to acknowledge NSF (DMR-1453083) for financial support for this research. NM EPSCoR (NSF Grant No. IIA-1301346) and USDA (NIFA 2015-38422-24059) are acknowledged for partially supporting the research. The Bruker X-ray diffractometer was purchased via a National Science Foundation CRIF:MU award to the University of New Mexico (CHE 04-43580). All computations were carried out at the Center for Functional Nanomaterials, Brookhaven National Laboratory, which is supported by the U.S. Department of Energy, Office of Basic Energy Sciences, under contract DE-SC0012704. J.J.R. acknowledges NSF (Grant CHE 1602240) for financial support.

■ REFERENCES

(1) *Handbook of Conducting Polymers*, 3rd ed.; Skotheim, T. A., Reynolds, J. R., Eds.; CRC Press: Boca Raton, FL, 2007.

(2) (a) Cheng, Y.-J.; Yang, S.-H.; Hsu, C.-S. *Chem. Rev.* **2009**, *109*, 5868−5923. (b) Zhang, Q.; Kan, B.; Liu, F.; Long, G.; Wan, X.; Chen, X.; Zuo, Y.; Ni, W.; Zhang, H.; Li, M.; Hu, Z.; Huang, F.; Cao, Y.; Liang, Z.; Zhang, M.; Russell, T. P.; Chen, Y. *Nat. Photonics* **2015**, *9*, 35−41. (c) Li, Y.; Guo, Q.; Li, Z.; Pei, J.; Tian, W. *Energy Environ. Sci.* **2010**, *3*, 1427−1436. (d) Beaujuge, P. M.; Fréchet, J. M. J. *J. Am. Chem. Soc.* **2011**, *133*, 20009−20029.

(3) (a) Jiang, B.; Yang, S. W.; Bailey, S. L.; Hermans, L. G.; Niver, R. A.; Bolcar, M. A.; Jones, W. E., Jr. *Coord. Chem. Rev.* **1998**, *171*, 365−386. (b) Kingsborough, R. P.; Swager, T. M. In *Progress in Inorganic Chemistry*; Karlin, K. D., Ed.; John Wiley & Sons, Inc.: Hoboken, NJ, 1999; Vol. *48*, pp 123−231. (c) Hirao, T. *Coord. Chem. Rev.* **2002**, *226*, 81−91. (d) Liu, Y.; Li, Y.; Schanze, K. S. *J. Photochem. Photobiol., C* **2002**, *3*, 1−23. (e) Moorlag, C.; Sih, B. C.; Stott, T. L.; Wolf, M. O. *J. Mater. Chem.* **2005**, *15*, 2433−2436. (f) Choy, W. C. H.; Chan, W. K.; Yuan, Y. *Adv. Mater.* **2014**, *26*, 5368−5399.

(4) (a) Jørgensen, M.; Carlé, J. E.; Søndergaard, R. R.; Lauritzen, M.; Dagnæs-Hansen, N. A.; Byskov, S. L.; Andersen, T. R.; Larsen-Olsen, T. T.; Böttiger, A. P. L.; Andreasen, B.; Fu, L.; Zuo, L.; Liu, Y.; Bundgaard, E.; Zhan, X.; Chen, H.; Krebs, F. C. *Sol. Energy Mater. Sol. Cells* **2013**, *119*, 84−93. (b) Kang, H.; Kim, G.; Kim, J.; Kwon, S.; Kim, H.; Lee, K. *Adv. Mater.* **2016**, *28*, 7821−7861. (c) Hu, Z.; Ying, L.; Huang, F.; Cao, Y. *Sci. China: Chem.* **2017**, *60*, 571−582.

(5) (a) Köhler, A.; Wittmann, H. F.; Friend, R. H.; Khan, M. S.; Lewis, J. *Synth. Met.* **1994**, *67*, 245−249. (b) Köhler, A.; Wittmann, H. F.; Friend, R. H.; Khan, M. S.; Lewis, J. *Synth. Met.* **1996**, *77*, 147−150. (c) Wilson, J. S.; Köhler, A.; Friend, R. H.; Al-Suti, M. K.; Al-Mandhary, M. R. A.; Khan, M. S.; Raithby, P. R. *J. Chem. Phys.* **2000**, *113*, 7627−7634. (d) Guo, F.; Kim, Y.-G.; Reynolds, J. R.; Schanze, K. S. *Chem. Commun.* **2006**, 1887−1889. (e) Glusac, K.; Köse, M. E.; Jiang, H.; Schanze, K. S. *J. Phys. Chem. B* **2007**, *111*, 929−940. (f) Wong, W.-Y.; Ho, C.-L. *Acc. Chem. Res.* **2010**, *43*, 1246−1256. (g) Wong, W.-Y.; Harvey, P. D. *Macromol. Rapid Commun.* **2010**, *31*, 671−713. (h) Ho, C.-L.; Wong, W.-Y. *Coord. Chem. Rev.* **2011**, *255*, 2469−2502. (i) Hsu, H.-Y.; Vella, J. H.; Myers, J. D.; Xue, J.; Schanze, K. S. *J. Phys. Chem. C* **2014**, *118*, 24282−24289.

(6) (a) Wong, W.-Y.; Wang, X.-Z.; He, Z.; Djurisic, A. B.; Yip, C.-T.; Cheung, K.-Y.; Wang, H.; Mak, C. S. K.; Chan, W.-K. *Nat. Mater.* **2007**, *6*, 521−527. (b) Wong, W.-Y.; Wang, X.-Z.; He, Z.; Chan, K.-K.; Djurisic, A. B.; Cheung, K.-Y.; Yip, C.-T.; Ng, A. M.-C.; Xi, Y. Y.; Mak, C. S. K.; Chan, W.-K. *J. Am. Chem. Soc.* **2007**, *129*, 14372−14380. (c) Baek, N. S.; Hau, S. K.; Yip, H.-L.; Acton, O.; Chen, K.-S.; Jen, A. K.-Y. *Chem. Mater.* **2008**, *20*, 5734−5736. (d) Wu, P.-T.; Bull, T.; Kim, F. S.; Luscombe, C. K.; Jenekhe, S. A. *Macromolecules* **2009**, *42*, 671−681.

(7) (a) Wong, W.-Y.; Wang, X.; Zhang, H.-L.; Cheung, K.-Y.; Fung, M.-K.; Djurišić, A. B.; Chan, W.-K. *J. Organomet. Chem.* **2008**, *693*, 3603−3612. (b) Mei, J.; Ogawa, K.; Kim, Y.-G.; Heston, N. C.; Arenas, D. J.; Nasrollahi, Z.; McCarley, T. D.; Tanner, D. B.; Reynolds, J. R.; Schanze, K. S. *ACS Appl. Mater. Interfaces* **2009**, *1*, 150−161. (c) Zhan, H.; Lamare, S.; Ng, A.; Kenny, T.; Guernon, H.; Chan, W.-K.; Djurišić, A. B.; Harvey, P. D.; Wong, W.-Y. *Macromolecules* **2011**, *44*, 5155−5167. (d) He, W.; Jiang, Y.; Qin, Y. *Polym. Chem.* **2014**, *5*, 1298−1304.

(8) He, W.; Livshits, M. Y.; Dickie, D.; Yang, J.; Quinnett, R.; Rack, J. J.; Wu, Q.; Qin, Y. *Chem. Sci.* **2016**, *7*, 5798−5804.

(9) Schröder, N.; Lied, F.; Glorius, F. *J. Am. Chem. Soc.* **2015**, *137*, 1448−1451.

(10) Pawle, R. H.; Agarwal, A.; Malveira, S.; Smith, Z. C.; Thomas, S. W. *Macromolecules* **2014**, *47*, 2250−2256.

(11) Kim, H. G.; Jo, S. B.; Shim, C.; Lee, J.; Shin, J.; Cho, E. C.; Ihn, S.-G.; Choi, Y. S.; Kim, Y.; Cho, K. *J. Mater. Chem.* **2012**, *22*, 17709.

(12) Lin, Y.-Z.; Yeh, C.-W.; Chou, P.-T.; Watanabe, M.; Chang, Y.-H.; Chang, Y. J.; Chow, T. J. *Dyes Pigm.* **2014**, *109*, 81−89.

(13) Dubinina, G. G.; Price, S. C.; Abboud, K. A.; Wicks, G.; Wnuk, P.; Stepanenko, Y.; Drobizhev, M.; Rebane, A.; Schanze, K. S. *J. Am. Chem. Soc.* **2012**, *134*, 19346−19349.

(14) Wang, L.; Huang, W.; Li, R.; Gehrig, D.; Blom, P. W. M.; Landfester, K.; Zhang, K. A. I. *Angew. Chem., Int. Ed.* **2016**, *55*, 9783−9787.

(15) Bhanvadia, V. J.; Patel, H. A.; Sharma, N. N.; Patel, A. L. *Synth. Commun.* **2016**, *46*, 1052−1061.

(16) Chen, M.; Moad, G.; Rizzardo, E.; Evans, R. A.; Haeussler, M. Conducting and semiconducting organic materials. Int. Patent WO2009155657A1, 2009.

(17) (a) Casida, M. E. In *Recent Advances in Density Functional Methods*; Chong, D. P., Ed.; World Scientific Publishing Co. Ltd.: Singapore, 1995; p 155. (b) Bauernschmitt, R.; Ahlrichs, R. *Chem. Phys. Lett.* **1996**, *256*, 454−464.

(18) Frisch, M. J.; Trucks, G. W.; Schlegel, H. B.; Scuseria, G. E.; Robb, M. A.; Cheeseman, J. R.; Scalmani, G.; Barone, V.; Petersson, G.

A.; Nakatsuji, H.; Li, X.; Caricato, M.; Marenich, A.; Bloino, J.; Janesko, B. G.; Gomperts, R.; Mennucci, B.; Hratchian, H. P.; Ortiz, J. V.; Izmaylov, A. F.; Sonnenberg, J. L.; Williams-Young, D.; Ding, F.; Lipparini, F.; Egidi, F.; Goings, J.; Peng, B.; Petrone, A.; Henderson, T.; Ranasinghe, D.; Zakrzewski, V. G.; Gao, J.; Rega, N.; Zheng, G.; Liang, W.; Hada, M.; Ehara, M.; Toyota, K.; Fukuda, R.; Hasegawa, J.; Ishida, M.; Nakajima, T.; Honda, Y.; Kitao, O.; Nakai, H.; Vreven, T.; Throssell, K.; Montgomery, J. A., Jr.; Peralta, J. E.; Ogliaro, F.; Bearpark, M.; Heyd, J. J.; Brothers, E.; Kudin, K. N.; Staroverov, V. N.; Keith, T.; Kobayashi, R.; Normand, J.; Raghavachari, K.; Rendell, A.; Burant, J. C.; Iyengar, S. S.; Tomasi, J.; Cossi, M.; Millam, J. M.; Klene, M.; Adamo, C.; Cammi, R.; Ochterski, J. W.; Martin, R. L.; Morokuma, K.; Farkas, O.; Foresman, J. B.; Fox, D. J. *Gaussian 09*, revision D. 1; Gaussian Inc.: Wallingford, CT, 2009.

(19) Hay, P. J.; Wadt, W. R. *J. Chem. Phys.* **1985**, *82*, 299−310.

(20) Tomasi, J.; Mennucci, B.; Cammi, R. *Chem. Rev.* **2005**, *105*, 2999−3094.

(21) Dreuw, A.; Head-Gordon, M. *J. Am. Chem. Soc.* **2004**, *126*, 4007−4016.

(22) Pope, M.; Swenberg, C. E. *Electronic Processes in Organic Crystals and Polymers*; Oxford University Press: New York/Oxford, 1999.

(23) Caspar, J. V.; Sullivan, B. P.; Kober, E. M.; Meyer, T. J. *Chem. Phys. Lett.* **1982**, *91*, 91−95.

(24) (a) Spano, F. C. *Acc. Chem. Res.* **2010**, *43*, 429−439. (b) Spano, F. C.; Silva, C. *Annu. Rev. Phys. Chem.* **2014**, *65*, 477−500.

(25) Chen, Z.; Hsu, H.-Y.; Arca, M.; Schanze, K. S. *J. Phys. Chem. B* **2015**, *119*, 7198−7209.

(26) Martin, R. L. *J. Chem. Phys.* **2003**, *118*, 4775−4777.

(27) Murgatroyd, P. N. *J. Phys. D: Appl. Phys.* **1970**, *3*, 151−156.

(28) (a) Liu, F.; Zhou, Z.; Zhang, C.; Vergote, T.; Fan, H.; Liu, F.; Zhu, X. *J. Am. Chem. Soc.* **2016**, *138*, 15523−15526. (b) Chen, W.; Zhang, Q. *J. Mater. Chem. C* **2017**, *5*, 1275−1302. (c) Dai, S.; Zhao, F.; Zhang, Q.; Lau, T.-K.; Li, T.; Liu, K.; Ling, Q.; Wang, C.; Lu, X.; You, W.; Zhan, X. *J. Am. Chem. Soc.* **2017**, *139*, 1336−1343.

(29) (a) Tao, Y.; Yuan, K.; Chen, T.; Xu, P.; Li, H.; Chen, R.; Zheng, C.; Zhang, L.; Huang, W. *Adv. Mater.* **2014**, *26*, 7931−7958. (b) Im, Y.; Kim, M.; Cho, Y. J.; Seo, J.-A.; Yook, K. S.; Lee, J. Y. *Chem. Mater.* **2017**, *29*, 1946−1963.

DOI: 10.1021/jacs.7b05801
J. Am. Chem. Soc. 2017, 139, 14109−14119